Organoid-based modeling of platinum resistance identifies KRT17 as both a response mediator and biomarker for targeted therapy in ovarian cancer

Juliane Reichenbach[1,2], Juliana Schmid[1], Sophia Hierlmayer[1], Tingyu Zhang[1], Ilaria Piga[4], Sophia Geweniger[1], Jonas Fischer[1], Aarushi Davesar[1], Nemanja Vasovic[1], Anca Chelariu-Raicu[1,2,3], Fabian Kraus[1], Alexander Burges[1], Bastian Czogalla[1,3], Doris Mayr[5], Tobias Straub[6], Christoph Klein[7], Jesper V. Olsen[4], Sven Mahner[1,2,3], Fabian Trillsch[1,2,3] and Mirjana Kessler[1,2,3]*

Affiliations:
1) Department of Obstetrics and Gynecology, University Hospital, Ludwig-Maximilians-University Munich, Munich, Germany
2) Bavarian Cancer Research Center (BZKF), Munich, Germany
3) German Cancer Consortium, DKTK, Partner Site Munich, Heidelberg, Germany
4) Proteomics Program, Faculty of Health and Medical Sciences, Novo Nordisk Foundation Center for Protein Research, University of Copenhagen, Copenhagen, Denmark
5) Department of Pathology, LMU Munich, 80337 Munich, Germany
6) Bioinformatics Unit, Biomedical Center, LMU Munich, Martinsried, Germany.
7) Department of Pediatrics, Dr. Von Hauner Children's Hospital, University Hospital, Ludwig-Maximilians-University Munich, 80337 Munich, Germany

*Corresponding author: Mirjana.kessler@med.uni-muenchen.de
ORCID: https://orcid.org/0000-0002-9879-1052

Summary

Variable platinum responses drive high mortality in high-grade serous ovarian cancer (HGSOC), but to date, there is no molecular approach to define resistance levels for clinical decision-making. Here, we developed the organoid drug resistance assay (ODR-test) with patient-derived organoids from our ovarian cancer biobank and found that all HGSOC patients develop molecular resistance under exposure to carboplatin, although with varying clinical implications. Sustained phenotypic reprogramming and cellular plasticity under carboplatin pressure emerged as a conserved mechanism irrespective of the basal resistance level. Transcriptional and proteomic analyses revealed changes in cell adhesion and differentiation in post-platinum lines as adaptive responses that drive the increase in resistance. We identified Keratin 17 (KRT17) as a mediator of developing platinum resistance and validated its function by CRISPR/Cas9 and overexpression. Additionally, we found that KRT17 expression status (K-score) is a significant negative prognostic histopathological biomarker in a large cohort (N=384) of advanced HGSOC patients. In organoids, increased KRT17 levels enhanced sensitivity to PI3K/Akt inhibitors Alpelisib and Afuresertib, highlighting the potential of KRT17 as a stratification biomarker for targeted therapies.

45

KEYWORDS

47

48 ovarian cancer; platinum-resistance; patient-derived organoids; drug-resistance testing; KRT17;
49 Prognostic biomarkers, targeted therapy
50

INTRODUCTION

52

53 The pronounced heterogeneity of high-grade serous ovarian cancer (HGSOC) challenges the
54 development of targeted therapies, leaving platinum-based chemotherapy as the main backbone of
55 treatment [1]. However, while initially effective in the vast majority of patients, its therapeutic benefits
56 diminish over time, as tumors acquire resistance, resulting in highly variable response rates among
57 patients [2][3]. In recurrent disease, the decision regarding platinum re-administration still relies only on
58 clinical and chronological criteria due to the absence of molecular predictive and stratification tools [4].
59 Consequently, many patients receive ineffective therapy, and therapeutic options remain limited [5].
60 Despite extensive research into the molecular adaptions that tumors undergo during platinum
61 treatment, preclinical studies have not yet yielded clinically applicable results [6][7]. As an important
62 advancement to standard cell lines and cell line-based xenograft models, patient-derived organoids
63 (PDOs) of HGSOC maintain the epithelial structure, allow long-term cultivation, and preserve the full
64 genomic and functional hallmarks of ovarian cancer [8–11]. Thus, an HGSOC PDO biobank from a large
65 heterogeneous prospective patient cohort with well-documented clinical data provides a unique
66 resource for studying individual differences in platinum response and the emergence of resistant
67 phenotypes [12].
68 Standard viability-based *in vitro* drug assays quantify only the direct cytotoxicity of chemotherapy by
69 measuring the cell viability after exposure [13]. However, since therapy in patients likely drives selection
70 mechanisms within a tumor that allows the expansion of pre-existing minor clones, viability testing is
71 inadequate for capturing this critical aspect of drug response [14][15].
72 Understanding the role of changes in tumor stemness and cell biology over time is critical to unraveling
73 the mechanisms of platinum resistance. Transcriptional profiling of the fallopian tube epithelium, the
74 origin of HGSOC [16], revealed subclusters of cells with stem cell signatures [17–20]. Among these, the type
75 I intermediary cytoskeletal filament protein Keratin 17 (KRT17) has been identified as one of the
76 markers of the progenitor population [17–20]. In other epithelial tissues, KRT17 is studied for its role in
77 tissue regeneration and stress responses [21][22]. By activating the PI3K/Akt signaling cascade, KRT17
78 promotes stemness and cell fate change in keratinocytes [23]. Upregulated in various epithelial cancers,
79 including HGSOC, KRT17 correlates with poor clinical outcomes, cell proliferation, and therapy
80 resistance [24–34]. Notably, inhibition of the PI3K/Akt signaling cascade has been proposed to target
81 chemoresistance in ovarian cancer [35–37].
82 In this study, we have developed the *in vitro* Organoid Drug Resistance Test (ODR-test) to quantify the
83 effect of chemotherapy, in this case platinum, on cancer stemness potential. Long-term cultivation of
84 *post*-platinum-treated HGSOC PDOs enabled transcriptional and proteomic analyses of adaptive
85 changes under therapeutic pressure. We identified KRT17 as a mediator of platinum response and
86 validated our findings of a potential clinical prognostic impact in a large cohort of advanced HGSOC
87 patients. Notably, high KRT17 levels could stratify the use of PI3K/Akt-inhibitors in HGOSC treatment,

88   with organoids that overexpressed KRT17 showing improved sensitivity to the PI3K-inhibitor Alpelisib
89   and Akt-inhibitor Afuresertib. These findings pave the way for the identification of platinum-resistant
90   ovarian cancer using biomarkers and for individualized, molecular-based treatment strategies that
91   improve the management following suboptimal responses to platinum chemotherapy.
92
93
94
95   **RESULTS**
96
97   **The Organoid-Drug-Resistance Test**
98
99   Primary tumor tissue from HGSOC patients, obtained during ovarian cancer debulking surgeries was
100 processed and patient-derived organoid (PDO) lines were generated as described previously within
101 our ovarian cancer organoid biobank [12]. To investigate patient-specific platinum responses, we
102 selected four organoid lines (HGSOC_06, HGSOC_08, HGSOC_14, and HGSOC_20) from patients with
103 documented clinical backgrounds (Table S1). All PDO lines demonstrated stable growth patterns,
104 maintaining stable stem cell potential *in vitro*, with expandability over 20 passages for more than six
105 months (Fig. 1A).
106 Initially, we quantified the response of organoids to carboplatin by measuring the change in cell
107 viability after 72 h, normalized to the control, and determined IC50 values for each patient-specific
108 organoid line (Fig. 1B, C). The IC50 represents the concentration of carboplatin required to achieve a
109 50 % reduction of cell viability.
110 Notably, PDOs consist of cells at various stages of differentiation, with the progenitor population
111 playing a key role in long-term cancer growth. Given that the residual growth potential of
112 chemotherapy-surviving cancer cells presents the main challenge for strategies preventing recurrence,
113 we focused on identifying sustained changes in organoids caused by sublethal carboplatin exposure.
114 Therefore, we have designed the Organoid Drug Resistance (ODR)-test to identify and quantify the
115 potential changes in stemness capacity as a consequence of drug treatment. In brief, PDO lines were
116 exposed 48 h to carboplatin at five different concentrations (6.25 µM, 12.5 µM, 25 µM, 50 µM, and
117 100 µM) alongside a control, followed by a 72 h recovery phase and were subsequently passaged (P1)
118 to a multiwell format in technical triplicates (Fig. 1D). The Growth Permitting Concentration (GPC) was
119 defined as the highest concentration of carboplatin at which organoids maintained their stemness,
120 assessed by their unlimited expansion potential, serving as a measure of patient-specific platinum
121 resistance. While signs of acute cellular stress were notable right after the 72 h recovery (P0) (increase
122 in granularity, dark appearance loss of adhesion, Fig. 1E and Fig.S1A), the functional impact of
123 carboplatin on the organoid regeneration potential could be assessed only after singularization and
124 reseeding (Fig. 1F). Compared to the previously determined IC50 values, the GPCs determined by the
125 ODR-test were in three cases substantially lower (Fig. 1G). This implies that for these tumors a much
126 lower platinum concentration is sufficient to exhaust long-term growth potential, than the one
127 necessary to reduce overall viability to 50%. We observed a consistent trend of decreasing organoid
128 formation potential with increasing concentrations of carboplatin in all donors. The number and size
129 of the organoids in P1 were quantified by analysis of phase contrast images from independent wells in
130 replicates. The magnitude of reduction in organoid count in P1 varied significantly between the lines,
131 indicating substantial individual differences in their capacity to withstand platinum challenge (Fig. 1H).

132   The surface area of individual organoids was determined with the Qupath software annotation tool [38]
133   (Fig. S1B, S1C). Surface size distribution analysis revealed that, despite a reduction in organoid
134   formation efficiency, the mean size of the organoids that regrew in P1 remained stable until the GPC
135   was reached (Fig. 1I). In line with this, at concentrations higher than the GPC, organoids were smaller
136   and could not be further expanded (Fig. 1I, Fig. S 1D). Although initially viable, these 3D cellular
137   aggregates effectively lost regeneration potential two to three weeks after carboplatin exposure.
138   Importantly, organoids that regrew in P1 at GPC concentration despite a lower count in comparison to
139   the control line could be successfully passaged in long-term culture (>3 months), with expansion
140   potential comparable to that of *non*-treated controls (Fig. 1J). In conclusion, ODR testing determined
141   a patient-specific critical concentration of platinum (GPC) required to effectively exhaust the stemness
142   potential of HGSOC organoids. Average organoid size, rather than organoid count, after the challenge
143   is a more suitable criterion to predict long-term growth capacity. Four ptGPC1 lines (post-treatment at
144   GPC growing) from different donors were successfully established with continued stable growth in
145   culture, confirming full preservation of growth capacity several months after carboplatin treatment.
146
147   **Phenotypic reprogramming in post-platinum organoids**
148
149   The robust expandability of the ptGPC1 lines after the ODR-test provided the opportunity to compare
150   them to respective untreated control PDO lines. The repair process of the double-stranded DNA breaks
151   is coordinated by phosphorylated Histone protein A2X (yH2AX), initiating the recruitment of other
152   repair proteins to the damage site, including BRCA1 [39,40]. On average, more than two months passed
153   since the exposure to carboplatin. Notably, ptGPC1 PDO lines still exhibited sustained elevated yH2Ax
154   and pBRCA1 phosphorylation, as detected by confocal imaging, (Fig. 2A). Meanwhile, expression levels
155   of stemness-related pathways, including Wnt and BMP target genes, as well as regulators of lineage
156   fidelity and differentiation (PAX8, FOXM1, and CD133), analyzed by qPCR, showed no consistent
157   changes in regulation among the different WT/ptGPC1 line pairs (Fig. 2B). The expression levels of ID2
158   and ID3, which are downstream of active BMP signaling, remained relatively stable and robust, as
159   indicated by low ΔCt values (Fig. S 1E). This aligns with the preserved growth capacity of ovarian cancer
160   PDOs, as BMP activity is known to promote their growth [8,12]. Despite preserved growth capacity,
161   ptGPC1 organoids showed changes in cellular architecture visualized by actin stain phalloidin as well
162   as prominent defects in the morphology of the nuclei (Fig 2C). The expression pattern of the nucleolus
163   marker fibrillarin was found to be a more condensed and larger area in comparison to controls (Fig.
164   2D). These findings suggest that carboplatin induces irreversible molecular changes in organoids
165   without impairing the general ability of cell proliferation and progenitor potential.
166   To further evaluate whether the observed cellular phenotype in ptGPC1 organoids plays a functional
167   role in response to the platinum challenge, we subjected them to a second round of carboplatin
168   treatment and ODR testing (ODR2-test) using the same workflow (Fig. 2E). We found that organoids
169   that underwent re-challenge showed notably improved formation and growth potential after the
170   second treatment when compared with the outcomes from ODR1-test (Fig. 2F, Fig. S 2A-D). For all
171   tested lines the growth-permitting concentration of the second challenge - defined as GPC2 -
172   surpassed the previous GPC1 value (Fig. 2G). Importantly, for each line and at every carboplatin
173   concentration, organoid counts were consistently higher post-ODR2 compared to post-ODR1 counts
174   resulting in enhanced ODR-response profiles (Fig. 2H). In summary, repeated *in vitro* platinum
175   treatment and ODR testing revealed the gradual development of resistance in PDO organoids,
176   including those derived from patients with clinically favorable platinum responses.

177

Cytoskeleton remodeling promotes platinum resistance

179

180   Next, we aimed to gain a deeper understanding of the biology of ptGPC organoid lines by evaluating
181   their transcriptomic and proteomic landscapes, to obtain a global view of the therapy-driven long-term
182   changes. Bulk RNA sequencing of two paired donor PDO lines (HGSOC_06 and HGSOC_08), with
183   additional biological replicates (*non*-treated and ptGPC lines) revealed a strong patient-specific
184   component in the expression profiles, as visualized by principal component analysis (PCA), with
185   carboplatin treatment not having a defining impact on the overall gene expression profile (Fig. 3A).
186   This great interpatient heterogeneity is in line with previously published scRNA data from ovarian
187   cancer tumor tissue [41]. Differential expression analysis performed with the DESeq2 R package
188   identified 837 genes differentially regulated in ptGPC1 lines (p-value <0.05), among which 80 were
189   significant in adjust < 0.05 analysis (Table S2). The Volcano plot of the differentially expressed genes
190   (*non*-treated vs. ptGPC lines) revealed the most strongly regulated candidates (Log2Foldchange, and
191   p-value) in response to chemotherapy (Fig. 3B). Despite a pronounced difference between the two
192   donors, reflected also in their clinical background, the set of genes showed a consistent pattern of
193   change in expression driven by carboplatin treatment. As illustrated by heat-map analysis of the top
194   25 regulated genes based on their significance (p-adjust < 0.05), samples clustered according to the
195   treatment, confirming the existence of a common signature response of the organoids upon
196   carboplatin exposure (Fig. 3C). The Gene Set Enrichment Analyses (GSEA) of regulated genes for GO:
197   Biological Processes revealed significant positive enrichment or upregulation in gene sets involved in
198   tissue and epithelial development and differentiation, while cell adhesion regulators were found
199   downregulated in ptGPC1 organoids (Fig. 3D). Mass spectrometry analysis of the protein lysates of the
200   same pair of organoid lines in quadruplicates confirmed key findings of the transcriptional profiling,
201   with highly similar sample distribution in the PCA plot (Fig. 3E). Likewise, GSEA for Biological Processes
202   showed significant enrichment in pathways regulating migration and cell adhesion (Fig 3F). On the
203   proteome level, a total of 947 (p-adjust < 0.05) proteins were confirmed to be regulated in the same
204   fashion in both donors (Table S3). The enrichment score plots (ES) for the downregulation of adhesion-
205   related signatures in transcriptomic and proteomic data sets yielded comparable results providing
206   complementary evidence obtained by independent omics methodologies of the downregulation of
207   adhesion complexes in ptGPC organoids (Fig 3F, G).
208   Remodeling of the cytoskeleton and changes in adhesion have previously been found to promote
209   therapy resistance. Downregulation of vimentin, one of the main regulators of mechanosensing [42] has
210   been reported in ovarian cancer cell line models during the acquisition of resistance [43,44]. Accordingly,
211   a reduction of vimentin signal intensity was detected by confocal imaging in our organoid ptGPC model
212   (Fig 3H), validating the RNA sequencing data, since vimentin was one of the top downregulated genes
213   as visualized in the heat-map (Fig. 3C).
214   Considering the significant changes in genes regulating cytoskeletal organization detected in the
215   transcriptome of ptGPC lines, along with previous studies linking KRT17 to the stemness compartment
216   of the fallopian tube and ovarian cancer [17–20], we investigated whether KRT17 has a functional role in
217   the development of platinum resistance. Though initially below the (p-adjust) threshold in bulk RNA
218   profiling, transcriptional upregulation in KRT17 organoids in response to carboplatin and subsequent
219   ODR-testing was confirmed by qPCR for four independent ptGPC1 paired samples of different donors
220   (Fig. 3I). Congruently, a rise in KRT17 levels in ptGPC1 organoids were visualized by confocal imaging
221   (Fig. 3J).

222

Functional KRT17 overexpression increases the platinum resistance of the organoids

224

225 To assess the functional relevance of KRT17 in the process of increasing resistance, we edited the
226 KRT17 gene locus using CRISPR/Cas9, introducing specific gRNAs by nucleofection, followed by the
227 generation of a monoclonal line. Editing resulted in the efficient excision of 96 bases in exon 4, as
228 confirmed by Sanger sequencing (Fig. S 3A-C) qPCR analysis of the expression of individual exons of
229 the KRT17 gene, in the crKRT17 HGSOC_08 line confirmed the complete loss of exon 4 expression,
230 while all other tested exons showed preserved transcription levels (Fig. 4A). In alignment, Western
231 Blot revealed a truncated KRT17 protein at ~ 40 kDa, with the absence of a full-length protein in the
232 CRISPR/Cas9-engineered donor line (Fig. 4B).
233 We then investigated whether truncation of the KRT17 protein influences the response of organoids
234 to carboplatin by ODR testing. Compared to the WT ptGPC lines, crKRT17 ptGPC lines exhibited strongly
235 increased resistance to consecutive carboplatin treatment (two rounds of ODR-testing), as organoids
236 regrew in P1 following the exposure to maximal (100 μM) carboplatin concentration (Fig. 4C, Fig. S 3D,
237 E). Consequently, GPC1 and GPC2 levels were higher in the crKRT17 line (GPC1 25 μM, GPC2 100 μM),
238 when compared to the WT line (GPC1 12.5 μM, GPC2 25 μM) (Fig. 4D). Notably, quantification of the
239 KRT17 gene expression level in crKRT17 ptGPC2 organoids compared to WT controls detected a strong
240 upregulation in the transcripts from remaining exons following repeated carboplatin treatment,
241 suggesting the existence of synergistic mechanisms between the effect of carboplatin and regulation
242 of the KRT17 gene locus (Fig. 4E). To confirm the upregulation of KRT17 at the protein level and specific
243 truncation at the peptide level, we performed a DIA-based proteomics experiment. The results showed
244 an overall increase in total KRT17 intensity in crKRT17 *non*-treated and ptGPC2 lines in comparison to
245 WT counterparts which fully aligned with qPCR data. Notably, we found one peptide DAEDWFFSK, that
246 corresponds to the genomic deletion in exon 4, that has significantly lower or absent MS/MS intensity
247 in the edited line (Fig. 4F) (p-value =1.6×10^{-6} and p value=1.24×10^{-9} for control and ptGPC lines
248 respectively). At the same time, platinum treatment further strongly boosted levels of all other KRT17
249 peptides in the crKRT17 lines (total protein) (p-value=8.19×10^{-9} and p=1.23×10^{-8}), and upregulation
250 was confirmed for all individual exons (Fig. S 3F). An additional strong increase in KRT17 levels,
251 triggered by edit was also confirmed by confocal imaging (Fig. 4G). Further, hyper-resistant crKRT17
252 ptGPC2 organoids exhibited an increase in KRT5 expression, a mediator of dedifferentiation and
253 marker of epithelial stages of increased plasticity [45], as well as in the distribution of the occludin
254 staining to basolateral membranes indicating further loss of polarity (Fig. 4H, I).
255 As CRISPR/Cas9 editing failed to achieve full knockout of KRT17 suggesting the potential existence of
256 selection pressure favoring edits where gene expression is partially maintained, we have chosen a
257 complementary approach and alternative strategy to prove the direct ability of KRT17 to modulate
258 carboplatin response. Full-length (Myc-DDK tagged) KRT17 was introduced by lentiviral transduction
259 (knock-in construct, KI) into a different PDO line (HGSOC_14) to additionally exclude donor-specific
260 effects (Fig. S 4A.) The protein expression from the KRT17 open reading frame was validated by both
261 Flag- antibody detecting the tagged protein (Fig. 4J) as well as with KRT17 antibody detecting both
262 endogenous and slightly larger Flag-Myc tagged KRT17 protein (double band). ODR-testing revealed
263 that expression of the exogenous KRT17 leads to a strong increase in the organoid count, in
264 comparison to the organoids transduced with the control vector (Fig. 4L). In agreement with this, GPC1
265 shifted from 25 μM to 50 μM in KRT17 (Fig 4L) transduced organoids confirming the ability of KRT17
266 to directly increase platinum resistance. Interestingly carboplatin treatment in the range of 12.5-25

6

267 µM, led to the appearance of significantly bigger, larger organoids in Flag KRT17 ptGPC1 lines in P1
268 (Fig. 4M), which subsequently translated into a strong increase in the growth rate of the KI-KRT17
269 organoids during subsequent passaging, quantified by splitting ratio (Fig. S 4C)

270

271 **K-Score is an independent negative prognostic factor of OS and PFS in HGSOC patients**

272

273 To investigate the association of KRT17 expression with clinical outcomes, we have conducted an
274 exploration analysis of clinical patient data to quantify the expression frequency of KRT17 across a high
275 number of HGSOC patients and to evaluate its prognostic impact. Therefore, tissue-microarrays (TMA)
276 of 384 patients diagnosed with primary HGOSC at advanced disease stages (FIGO III-IV) were stained
277 for KRT17 by immunohistochemistry. Clinical characteristics and descriptive statistics of the patient
278 cohort are listed in Table S4 and Table S5.
279 The evaluation of the KRT17 expression was conducted by digital AI-based imaging analysis [38] (Fig. S
280 4D). To quantify expression levels, we developed the K-score as a measure of the KRT17 expression,
281 which is based on the number of positively stained tumor cells in proportion to the overall detected
282 tumor cells and ranged between 0-200 % (Fig. 5A, Table S6). The average KRT17 expression across all
283 tested tumors was generally low, with a mean K-score of 2.82 % (Fig. S 4E). By using the biomarker
284 cutoff finder tool [46], we defined a K-score of 5 % as a benchmark to separate the populations of
285 KRT17^{high} and KRT17^{low} tumors. In Kaplan-Meier-analysis, the median overall survival for KRT17^{high}
286 patients was 21 months (95% CI 35.3-46.7 months) compared to 41 months (95% CI 11.1-30.9 months)
287 for KRT17^{low} patients (p=0.0043) (Fig. 5B). Median progression-free survival for KRT17^{high} patients was
288 14 months (95% CI 10.9-17.2 months) compared to 19 months (95% CI 17.1-20.9 months) for KRT17^{low}
289 patients (p=0.0081) (Fig. 5C). Cox regression multivariate analysis, controlled for the main factors
290 influencing the prognosis (general health status of the patients (ASA), age at first diagnosis,
291 postoperative residual disease and neoadjuvant chemotherapy) showed that the K-score is an
292 independent prognostic factor on overall survival with a Hazard ratio of 1.84 (CI 1.17-2.87) (Fig. 5D)
293 and progression free survival with a Hazard ratio of 1.58 (CI 1.06-2.34) (Fig. 5E). Taken together, the
294 data consistently showed that KRT17 not only has a functional role in the cellular response to platinum
295 in organoids, but its expression level in tumor tissue has prognostic significance in a large cohort of
296 advanced HGSOC patients, thus, making it a possible target for novel therapeutic approaches.

297

298 **KRT17 is a potential stratification marker for PI3K/Akt-pathway-targeted therapies**

299

300 KRT17's involvement in cellular stress response by activation of downstream signaling, including the
301 PI3K/Akt pathway has previously been reported in ovarian cancer models [23,37]. By now, the PI3K-
302 inhibitor Alpelisib and pan-Akt-inhibitor Afuresertib have shown tolerable safety profiles for the
303 treatment of HGSOC at the recurrent platinum-resistant stage but failed to reach primary endpoints
304 in studies designed to include all-comer study populations [47–49]. We tested whether a high KRT17
305 expression might be a potential stratification factor to determine which patients might benefit from
306 PIK3-Kinase- and/or Akt-inhibition. Therefore, we have exposed to platinum WT non-treated control
307 PDOs and WT ptGPC2 PDOs, crKRT17 platinum *non*-treated control PDOs, and crKRT17 ptGPC2 PDOs
308 with the PI3-kinase- and Akt-inhibitors Alpelisib and Afuresertib.
309 CrKRT17 *non*-treated control PDOs, overexpressing KRT17, were found to be more sensitive to Alpelisib
310 (IC50 9.89 µM vs. controls IC50 15.26), and the crKRT17 ptGPC2 PDOs showed the lowest IC50 value
311 of 5.77 µM, suggesting the additive effect of platinum treatment and crKRT17 edit, an effect which

312 was stable and reproducible in independent set of experiments (IC50 plot) (Fig. 5F). In the case of
313 Afuresertib, high levels of KRT17 induced sensitivity already in the crKRT17 *non*-treated control PDO
314 line (IC50 10.7 µM), without further reduction in the crKRT17 ptGPC2 line (IC50 9.17 µM, Fig. 5G).
315 Finally, we have validated the role of KRT17 in the response of organoids to Alpelisib, by treatment of
316 the KI-KRT17 line in comparison to control-transduced organoids which confirmed a strong increase in
317 sensitivity to Alpelisib (Fig. 5H).
318 These results demonstrated that elevated KRT17 levels and previous exposure to chemotherapy
319 predispose tumors to effective inhibition of PI3K signaling by Alpelisib, while pan-Akt inhibition by
320 Afuresertib primarily targets the KRT17 status irrespective of the carboplatin effect. In conclusion, the
321 KRT17 expression defined by the K-score status could be a valuable stratification tool to select patients
322 who could benefit from Akt-inhibitor treatment in advanced and platinum-treated HGSOC.
323
324

325 **DISCUSSION**
326
327 In the present study, we developed the ODR-test as a novel and innovative experimental approach to
328 quantify platinum resistance in ovarian cancer and study cellular plasticity which is driven by the
329 response to therapy. Although different groups previously reported an association between drug
330 resistance and enrichment of stemness-related phenotypes within tumors, the mechanism of how
331 chemotherapy resistance emerges remains poorly understood [15,50,51]. Since organoid growth in culture
332 is based on the preservation of epithelial progenitor potential, the ODR-test determines and quantifies
333 the conditions under which individual tumors can sustain growth capacity despite the damaging effects
334 of carboplatin. This represents an important conceptual advancement to commonly used drug assays
335 as they only determine the acute and direct toxic effects of the drugs on remaining viable cells [13,52].
336 Clinical experience has long suggested that every ovarian cancer patient develops molecular resistance
337 to repeated platinum treatment over time, even though the extent of resistance and the speed of the
338 process may vary between patients and could not be translated into a clinically applicable biomarker
339 stratification so far [5]. Importantly, the ODR-test effectively confirmed the existence of this
340 phenomenon *in vitro*, as organoids consistently exhibited an increase in resistance upon re-challenge
341 measured by a shift in the organoid count and an increase in growth permitting concentration (GPC)
342 regardless of their clinical outcome. The data is also fully consistent with the hypothesis that
343 carboplatin treatment triggers a conserved mechanism of the cellular response while the dynamics of
344 the resistance acquisition have a strong individual component that can be analyzed in detail in patient-
345 specific lines. Different degrees of resistance, observed in organoids after repeated ODR testing also
346 explain why increase does not carry clinical consequences in all cases, as the basal level of sensitivity
347 of each tumor is likely the result of complex genetic and environmental factors, and good responders
348 remain more sensitive despite a molecular drift towards a resistant phenotype.
349 Consequently, the ODR-test could be a useful tool to successfully address the challenge of identifying
350 patients at high risk for resistance development [4]. Global analysis of gene expression and the proteome
351 of ptGPC lines revealed changes in expression in cellular networks regulating cell adhesion, cell-cell
352 communication as well as cytoskeletal components (Figure 3A-G). The similarities in response of
353 different donor lines of variable basal resistance to carboplatin challenge are evidence of conserved
354 reprogramming mechanism and cellular plasticity under therapeutic pressure. While more research is
355 needed to fully understand the mechanisms of stemness preservation under platinum treatment, the
356 stable expansion of ptGPC lines offers a new valuable model to study this phenomenon. Identification
357 of KRT17 upregulation under carboplatin treatment is congruent with the findings of a previous study

358   showing that KRT17 is responsive to cytotoxic stressors such as platinum-induced DNA damage [53]. The
359   strong increase in platinum resistance profile that we detected in lines expressing elevated levels of
360   KRT17 by either CRISPR/Cas9 editing of exon 4 or through genomic integration of additional copies of
361   the KRT17 gene, demonstrated the ability of KRT17 to directly influence the response to carboplatin
362   and represents evidence of a potential regulatory loop. Altogether, these findings support the
363   hypothesis, that platinum-caused DNA damage induces KRT17, which subsequently actively
364   participates in changes in the cytoskeletal organization to enhance cellular stemness, promoting tumor
365   survival [23,34,37]. The clinical prognostic relevance of KRT17 expression was established by
366   immunohistochemical analysis of the KRT17 expression profile in a large cohort of 384 advanced
367   HGSOC patients. We found that the KRT17 expression level classified by the immunoreactive K-score,
368   has a significant prognostic value for both overall and progression-free survival. This clear prognostic
369   relevance, confirmed by the Cox proportional hazards model in combination with the *in vitro* results
370   on organoids, supports further studies and the development of the K-score as a biomarker in a clinical
371   context to determine which patients are likely to develop a platinum-resistant recurrent disease. As a
372   high KRT17 expression has been reported to have negative prognostic significance also in other
373   epithelial cancer entities, our study could be of interest in a broader oncological context [24–34].
374   Genetically modified organoids expressing high levels of KRT17 (ptGPC crKRT17 and KI KRT17 lines)
375   showing high levels of platinum resistance were a suitable model to study the response of ovarian
376   cancer to targeted agents as they reflect the potentially relevant clinical scenario of heavily pre-
377   treated, platinum-resistant, and highly KRT17-expressing tumors. In these organoids (Fig. 5F, G, H), we
378   have identified a strong improvement in sensitivity to the pan-Akt-inhibitor Afuresertib and PI3K-
379   inhibitor Alpelisib. This direct relationship between KRT17 expression and sensitivity of organoids to
380   Akt/PI3 kinase inhibition strongly suggests that further development of KRT17 as a promising
381   biomarker and stratification tool to implement therapies targeting Akt/PI3-kinase in the treatment of
382   platinum-resistant, recurrent ovarian cancer is warranted.
383   Patient-derived organoids effectively capture in vitro basic organization of the epithelial compartment
384   of the tumor tissue, as they expand in culture based on the balance of stemness and differentiation
385   mechanisms governing tumor growth. Though principal findings of the ODR testing and analysis of
386   ptGPC lines suggest that the model has sufficient complexity to phenocopy gradual rise in platinum
387   resistance observed in patients, the absence of immunosurveillance and tumor microenvironment
388   likely limits the predictive potential of the model regarding the timing of the disease recurrence, and
389   exact timing when the tumor will reach a resistance level which would be consequential for clinical
390   decision making. In line with this, while the K-score is significantly associated with negative patient
391   outcomes, it represents an indicator of a faster process of developing resistance during disease
392   progression.

393 **Acknowledgments**
394

Author Contributions

410
411 Conceptualization, M.K, and J.R.; methodology J.R, M.K., I.P, J.V.O; validation J.R., J.S, S.H, T.Z, S.G.;
412 formal analysis J.R, J.S, I.P., S.H., S.G, T.Z, A.D., J.V.O and M.K.; investigation J.R., J.S., S.H., T.Z., I.P, S.G,
413 J.F., A.C.R., A.D., and N.V.; resources S.M., C.K., F.T., A.B, B.C., F.K., D.M, T.S.; writing-original draft J.R.,
414 M.K.; writing-reviewer and editing J.R, M.K., F.T, S.M., F.K., B.C., D.M., A.B., T.S., C.K., I.P., J.V.O., S.G.,
415 J.S.; visualization J.R, J.S, S.G, I.P, and M.K.; supervision M.K. project administration M.K**.;** funding
416 acquisition M.K., F.T., J.R., A.C.R., J.V.O.

417

Declaration of interests

419
420 The authors report the following competing interests: SM obtained research funding, advisory board,
421 and honorary or travel expenses from AbbVie, AstraZeneca, Clovis, Eisai, GlaxoSmithKline, Hubro,
422 Immunogen, Medac, MSD, Novartis, Nykode, Olympus, PharmaMar, Pfizer, Roche, Seagen, Sensor
423 Kinesis, Teva. FT received research funding, advisory board, and honorary or travel expenses from
424 AbbVie, AstraZeneca, Eisai, GSK, ImmunoGen, MSD, Regeneron, Roche, and SAGA diagnostics. B.C.
425 received speech/advisory board honoraria from AstraZeneca and MSD. M.K. is listed as an inventor on
426 the patent for ovarian cancer organoid culture. Other authors have no competing interests.

Methods

428 Experimental model and study participants

429 Human subjects

430
431 The study was conducted following the Ethics Committee of the Ludwig-Maximilian-University (LMU),
432 Munich, Germany (17-0471), and in compliance with all legal EU, national, and local regulations. Each
433 patient provided written informed consent to participate. Ovarian cancer biobank, established
434 following our institutional protocols [12,54] was a source of primary high-grade serous ovarian cancer
435 patient-derived organoid (HGSOC PDO) lines that were used in this study including embedded tissue
436 samples, along with their clinical data. A routine pathological assessment of the primary tumor tissue
437 confirmed the malignant, non-borderline diagnosis based on standard histomorphology
438 characteristics. The samples were collected during multi-visceral surgeries at the Department for
439 Gynecology and Obstetrics, LMU Hospital, Munich, Germany. Our gyneco-oncological surgeons
440 collected clean peritoneal tumor deposits, avoiding macroscopically necrotic areas, and the tissue was
441 processed in our laboratory for organoid generation, as previously described [12,54]. Embedded tissue
442 and corresponding organoid cultures exhibit matching molecular profiles [8].

443 Tissue microarrays (TMA) for immunohistochemical analysis were prepared and stained by the LMU
444 Department of Pathology, comprising a total of 384 duplicated samples of HGSOC patients diagnosed
445 with advanced staged disease (FIGO III-IV) treated at our department. Clinical data was available for
446 further analysis.
447
448 Organoid cultivation
449
450 HGSOC PDOs were cultivated in individually optimized media according to the previously described
451 protocol. Donor lines included in the study all grew in OCM1 medium (low WNT, high BMP
452 environment) with two lines showing benefit from the addition of her 1β (Table S7) [12]. Passaging of
453 organoids cryopreservation and thawing procedures followed protocols established by our laboratory
454 [12]. Briefly, depending on organoid growth, every 10-20 days, organoids were released from Cultrex®
455 BME 2 and trypsinized with TrypLE™ (Gibco™). Depending on the grade of the desired dissociation,
456 the cell suspension was strained through cell filters to ensure singularization. Dissociated cells were
457 re-seeded in matrix ovarian cancer medium was added after 30 min of solidification. Cryopreservation
458 of organoids was performed in the proliferation phase of organoid growth in the first week *post*-
459 passage Organoids were pelleted and transferred to 1 ml Cryopreservation medium (e.g., Freezing
460 Medium Cryo-SFM, PromoCell – Human Centered Science®) and stored initially at -80°C freezing
461 container (e.g. Nalgene® Mr. Frosty, Sigma-Aldrich®), before transferring to liquid nitrogen for long-
462 term stable storage.
463
464 *In-vitro* Cell viability drug assay
465
466 Organoids were trypsinized, strained through the filter, and counted and 20-30,000 cells were seeded
467 in in a 48-well plate format in triplicates. At day 5-7 *post*-seeding, depending on the growth dynamic
468 of the individual line, fully formed organoids were treated with carboplatin at increasing
469 concentrations (dilution in organoid medium to 6.25 µM, 12.5 µM, 25 µM, 50 µM, and 100 µM),
470 alongside a control. The cell viability was measured after 72 h using the CellTiter-Glo® 3D Cell Viability
471 Assay (Promega) according to the manufacturer´s directions at the Varioskan™ LUX multimode
472 microplate reader (Thermo Scientific™). Drug response for PI3K/Akt inhibitors Alpelisib and Afuresertib
473 was measured in the same format with a treatment duration of five days. The individual inhibitory
474 concentration at 50 % cell viability was determined for each tested PDO line, in Graph Prism software
475 by calculating dose response by applying a nonlinear regression model.
476
477 Organoid Drug Resistance (ODR) test
478
479 The regenerative potential of organoids was tested by subjecting them to different doses of
480 carboplatin using our developed ODR test (Fig. 1D). Initially, organoids were singularized by
481 trypsinization, mechanical dissociation, and straining through a 200 µm filter for equal distribution and
482 seeded at density 50,000 cell/well in a 24-well plate format. At day 7 *post*-passage, the organoids were
483 treated with carboplatin for 48 h at five increasing concentrations (dilution in organoid medium to
484 6.25 µM, 12.5 µM, 25 µM, 50 µM, and 100 µM, alongside a control. After a 72-hour recovery phase in
485 a carboplatin-free organoid medium, passaging was performed to a 48-well format in a 1:3 ratio into
486 Passage 1 (P1). Organoid generation and growth were quantified by imaging each well at 4x and 10x

11

487 magnifications using a phase contrast microscope, at 3-, 7-, and 10-days post-split, and using the
488 annotation tool of Qupath Software. By further passaging of organoids, we identified the highest
489 carboplatin concentration level in P0 after which unlimited long-term expansion of the line was
490 possible permitting concentration (GPC).
491

492 RNA Isolation

493

494 The RNeasy Mini Kit (QIAGEN) was used for total RNA extraction according to the manufacturer′s
495 protocol. Organoids were released from the extracellular matrix with cold ADF++ and pelleted. After
496 resuspension in Buffer RLT (QIAGEN) supplemented with ß-mercaptoethanol and homogenization
497 70%-ethanol was added, and samples were processed via RNA purification columns. Quantification of
498 the RNA concentration and purity was performed with the Qubit 4 Fluorometer (Thermo Scientific™)
499 following the instructions of the Qubit™ RNA HS Assay Kit (Thermo Scientific™).
500

501 Reverse Transcription and qPCR

502

503 For the two-step quantitative reverse transcription PCR (qRT-PCR), the RNA samples were transcribed
504 to (cDNA) using the cDNA Synthesis Kit (Biozym). TaqMan® Universal PCR Master Mix, TaqMan® Gene
505 Expression Assay targeting the gene of interest (Table S8) was used for measuring quantitative gene
506 expression on the Applied Biosystems™ 7500 Fast Real-Time PCR System. The quantification of
507 expression levels was performed by ΔΔ Ct method relative to the expression of the Glycerinaldehyd-
508 3-phosphat-Dehydrogenase (GAPDH). Change of expression in the test group (e.g. ptGPC organoids)
509 was determined in relation to the average value of the expression of the gene in the control group.
510 The GraphPad Prism 10 software was used for data analysis and graphical representation.
511

512 CRISPR-Cas9 mediated editing of organoids

513

514 CRISPR-Cas9 mediated gene editing for KRT17 was performed with two customized single guide RNAs
515 (sgRNA) (Synthego) (Table S9). Organoids previously singularized by trypsinization and mechanic
516 dissociation were transfected with the Cas9 endonuclease and sgRNA /ribonucleoparticles (RNP) via
517 electroporation in the NEPA21 electroporator (Nepagene). For this purpose, 150,000 singularized
518 organoid cells each were combined in a total of 50 µl reaction mixture consisting of 25 µL reduced
519 serum medium (Opti-MEM™, Gibco™) and 25 µL assembled RNP mixture (1 µl SpCas9 2NLS Nuclease
520 (Synthego) (20 pmol/µl, 6 µl target-specific sgRNAs (30 pmol/µl) and 18 µl Opti-MEM™). Controls
521 included a positive control by transfection with sgRNA targeting the previously validated *TRAC* gene
522 (Human TRAC Positive Control, Synthego), and a negative (mock) control. After electroporation
523 organoids were resuspended in an OCM medium, pelleted and singularly seeded in Cultrex®.
524 Three weeks after electroporation, genomic DNA was extracted using the AllPrep DNA/RNA/protein
525 Kit (QIAGEN). and the targeted locus was amplified. Gel electrophoresis on 2 % agarose gels with SYBR
526 Safe DNA Gel Stain (Invitrogen) visualized the products alongside pBR328 Mix I (Carl Roth) as a DNA
527 marker. A purified PCR product was sent for Sanger sequencing to confirm the edit. Monoclonal
528 organoid lines have been generated by singularization of the pooled cultures, clones picking, and
529 expansion of the individual organoid lines.
530

531   Western Blot analysis

532

533   For the preparation of the total protein samples, organoids were harvested and washed with cold PBS.
534   The pellet was resuspended in 4x Laemmli buffer (Bio-Rad), volume adjusted with PBS to ensure 1x
535   Laemlli concentration, and lysates were heated for 10 min at 95°C. After SDS-PAGE, proteins were
536   transferred to 0.2 µM PVDF membrane by semi-dry Trans-Blot Turbo Transfer System (Bio-Rad),
537   followed by blocking in 3% milk powder and 1.5% BSA blocking solution. After overnight incubation
538   with the primary antibody at 4°C (Table S10) and 3 washing steps in TBS/Tween0.05%, the membrane
539   was incubated with the respective secondary HRP-conjugated IgG-antibody (Table S10) for 1 h at room
540   temperature. After washing, proteins were detected by use of the Cytiva Amersham™ ECL™ Prime
541   Western-Blot-Detection Reagent (Thermo Scientific™) on the ChemiDoc MP Imaging System (Bio-Rad).
542   ß-Actin (Sigma, A5441) Histone-2B (ab1790), or Histone-H3 (ab8580) antibodies were used as
543   endogenous control for the normalization of protein loading.

544

545   Lentiviral transduction

546

547   Ready-to-use lentiviral particles carrying FLAG (DDK)-Myc -agged full-length KRT17, or control vectors
548   (RC201619L1V and PS100064V) have been transduced following the established protocol[55].In short cell
549   culture plates (24-well format) were pre-coated with a 1:1 mixture of Cultrex and ADF medium and
550   left to solidify overnight at 37°C. Organoids were singularized and counted to calculate MOI. An
551   appropriate number of lentiviral KRT17 particles and a control vector were added to the suspension
552   with the addition of polybrene to facilitate the transduction, mixture was transferred to precoded
553   plates and incubated 24h at 37°C. The next day cells were retrieved and washed and 3D seeding was
554   performed, according to the standard organoid cultivation protocol. Successful transduction and
555   protein expression of the tagged KRT17 construct has been validated by Western Blotting.

556

557   RNA Sequencing and Data Analysis

558

559   Preparation of the library and NGS Sequencing of the RNA samples from carboplatin-treated and *non-*
560   treated ovarian cancer organoids, isolated by mRNA Easy (Qiagen) kit according to the 'manufacturer's
561   protocol, was performed by Novogene Co. Ltd. China, on the Illumina PE150 Novaseq platform,
562   fulfilling stringent quality control criteria (Q30 >95%). The reads were aligned against the index file
563   built from the GRCh38 primary assembly genome (GENCODE release 45) and quantified using the
564   Rsubread package (2.20.0), with the GRCh38 GENCODE v38 GTF file as the reference. Differential gene
565   expression analysis was performed using DESeq2 (version 1.46.0) in the R environment (version 4.4.2).
566   RStudio Packages DESeq2 (1.46.0), ggrepel (0.9.6), dplyr (1.1.4), pheatmap (1.0.12), clusterProfiler
567   (4.14.4), org.Hs.eg.db (3.20.0), AnnotationDbi (1.68.0), DOSE (4.0.0), enrichplot (1.26.05), ggplot2
568   (3.5.1) were used for the analysis and visualization of differential gene expression data.
569

570   Mass Spectrometry Analysis

571

572   Cell pellets were lysed in Eppendorf tubes with 50 µl of boiling lysis buffer (5% SDS, 100 mM Tris pH
573   8.5, 5 mM TCEP, and 10 mM CAA). The lysates were incubated at 95 °C for 10 min with mixing
574   (500 rpm) and quantified with Pierce BCA Protein Assay Kit (Thermo Scientific). Protein digestion was

13

575   performed using a Protein Aggregation Capture (PAC) [56]-based digestion MagReSyn Hydroxyl beads
576   (ReSyn Biosciences) on a King Fisher Flex system scientific (Thermo scientific).
577   Samples were mixed with beads were added to the samples at a protein beads ratio of 1:2. For each
578   sample, 200 µl of digestion solution (50 mM triethylammonium bicarbonate) containing Lys-C and
579   Trypsin at an enzyme-to-substrate ratio of 1:500 and 1:250, respectively. Digestion was performed
580   overnight at 37 °C. Protease activity was quenched by acidification with TFA to a final volume
581   percentage of 1% [57].
582   For proteome experiments, 500 ng of digested peptide were loaded in an Evotip Pure (Evosep)
583   following manufacturing instructions. Samples were analyzed using an Evosep column (PepSep EV-
584   1109, 8 cm - 150 µm - C18 1.5 µm) and a fused silica (EV-1087 - 20 µm) using an EASY-Spray™ source
585   and interfaced with the Orbitrap Astral Mass Spectrometer (Thermo Scientific). In all samples, spray
586   voltage was set to 1.8 kV, funnel RF level at 40, and heated capillary temperature at 275 °C. Samples
587   were separated on an Evosep One LC system using the pre-programmed gradient for 60 samples per
588   day (SPD – 21 minutes gradient). All experiments were acquired using a data-independent acquisition
589   (DIA) method, cycle time of 0.6 seconds, in a range of 480-1080 m/z, and a maximum injection time
590   (IT) of 30 ms.
591
592   Data analysis Proteomics
593
594   Raw files were analyzed in Spectronaut v19 (Biognosys) with a spectral library-free approach
595   (directDIA+) using the human protein reference 232 database (Uniprot 2022 release, 20,588
596   sequences) and 233 complemented with common contaminants (246 sequences).
597   Carbamidomethylation of cysteine was set as a fixed modification, whereas oxidation of methionine,
598   N-terminal protein acetylation was set as variable modifications. The enzyme/cleavage rule was set to
599   Trypsin/P, the digest type to specific, and a maximum number of two missed cleavages per peptide
600   was allowed. The maximum number of variable modifications per peptide was set to 5 and method
601   evaluation was turned off.
602   The data analysis of proteome data was performed in R version 4.4.0 (R Core Team (2021), R
603   foundation for statistical computing) with R Studio 2024.4.0.735. The output files were analyzed using
604   Rstudio with the following packages, dplyr (1.1.4), tidyverse, (2.0.0), ggrepel (0.9.6), Limma (3.60.6),
605   EnhancedVolcano (1.22.0), clusterProfiler (4.12.6), enrichplot (1.24.4), org.Hs.eg.db ('3.19.1).
606
607   Fixation and embedding of organoids
608
609   Fixation of organoids in Epredia™ Richard-Allan Scientific™ HistoGel™ (Thermo Scientific™) for
610   subsequent paraffin embedding, micro-sectioning, and staining procedures followed our institutional
611   protocol [12]. In summary, organoids were released from the Cultrex® BME 2 matrix by cold ADF++, fixed
612   in 4% Paraformaldehyde (PFA), and washed twice in PBS. Fixed organoids were gently resuspended in
613   100 µl of pre-heated HistoGel™, and the solidified HistoGel™ droplet was processed to paraffin
614   embedding and slicing.
615
616
617

Immunofluorescence staining of organoids and tissue

Immunofluorescence staining was performed as previously described [12]. In short, slides were deparaffinized in Roticlear® (Carl Roth), followed by rehydration in a descending ethanol series, antigen retrieval by heating in a steamer to 100°C with TRIS/EDTA-solution and permeabilization for 15 min in 1% Triton® X-100 (in PBS) solution (Sigma-Aldrich®). After blocking with 10 % serum, and primary antibody incubation at 4°C for at least 16 h, slides were stained with secondary IgG antibodies for 2 h at room temperature. DAPI counterstaining (Thermo Scientific™) visualized nuclei. Mowiol® 4-88 Water soluble Mounting Medium (Carl Roth) sealed the slides for imaging on a Leica SP8 confocal microscope.

Immunohistochemistry of TMA sections

After the removal of paraffine (Roticlear, and decreasing ethanol range), slides were incubated in antigen-retrieval solution pH 8,0 (Novocastra RE7116), for 2x 15 min in the heated Microwave and left to cool down for 20 min at room temperature. Next, samples were blocked for 10 min with Protein Block (Agilent Technologies, X0909). Primary antibody anti KRT17 (clone SPM560, ab 233912), diluted 1:250, was incubated for 1h at room temperature. After washing, (PH 7,5 TRIS buffer), samples were treated with AP Polymer anti-Mouse (Zytomed systems, ZUC-077) for 30 min, washed and Vector Red substrate was added for 20 min (Vector, SK-5100). Excess dye was washed out for 10 min under running water, counterstaining with Hematoxylin (Vector, H-3401) was performed for 10 sec and the washing step was repeated. Samples we mounted with Aquatex (Merck, 1.08562.0050).

TMA Staining evaluation

The ovarian cancer TMA slides were visualized by the automated Keyence Microscope BZ-X800 at a 20x magnitude with automated image stitching. The QuPath Bioimage Analysis Software [38] was used for IHC analysis of KRT17 expression on TMA slides. An automated script ensured accurate, consistent, and objective IHC scoring (Table S11). Stains were separated by color deconvolution after smoothing. QuPath´s Pixel and Object Classifier algorithms were interactively trained on more than 30 selected heterogeneous training images within the study collective to automatically annotate regions of interest and to distinguish epithelial tumor cells from all other detections. The QuPath´s Positive Cell Detection algorithm was applied for cell segmentation and counting. Intensity thresholds were determined for either negative, weakly positive, or strongly positive cells based on the cell KRT17 optical density sum (negative <0.09, weakly positive 0.09-0.17, strongly positive >0.17, Fig. 4D). Automated batch analysis was applied to all 384 duplicated TMA samples, providing data for further statistical analysis.

Statistical analysis

For the TMA analysis, the total cell count for tumor and stroma cells and positive cell detection were pooled for both sample duplicates before further statistical analysis. A tailored immunoreactivity score was established. For this purpose, weakly positive cell count was added to the twofold count of strongly positive cells, then divided by the total tumor cell count and multiplied by 100, resulting in a

662 range of 0 (all tumor cells negative for KRT17) to 200 (all tumor cells strongly positive for KRT17). We
663 named this adapted immunoreactivity score "K-score". Samples with less than 1150 detected tumor
664 cells in total were excluded from further statistical analysis, based on the required sample size to
665 classify the sample based on a 5% cutoff with >99,99% confidence. Clinical information, including data
666 about survival and disease progression, was related to the immunohistochemical scoring by descriptive
667 statistical analysis, Kaplan-Meier analysis, and Multivariate Cox regression analysis by the IBM SPSS
668 Statistical Software (version 29.0.1.0 (171)) as well as Survival (version 3.7.0) and survminer (0.5.0)
669 packages in R Data analysis and visualization by the web application *Cutoff Finder* [46] facilitated the
670 determination of an optimal cutoff point for patient stratification.
671
672 Data Visualization
673
674 Data visualization was performed using GraphPad Prism Software Version 10.1.1. software was used
675 to generate concentration-response curve diagrams for organoid counting and mRNA expression,
676 analyze cell viability data, and create graphical representations of the experimental results obtained
677 in Qupath (organoid count and surface area data). R packages survival, surminer, dplyr, foreign, and
678 ggplot2 were used for data processing and generating plots of survival analysis, and HR plots of Cox
679 proportional model analysis.
680

References

681
682 1. Ledermann, J. A. *et al.* ESGO–ESMO–ESP consensus conference recommendations on ovarian cancer:
683 pathology and molecular biology and early, advanced and recurrent disease☆. *Ann. Oncol.* **35**, 248–266 (2024).
684 2. Hanker, L. C. *et al.* The impact of second to sixth line therapy on survival of relapsed ovarian cancer
685 after primary taxane/platinum-based therapy. *Ann. Oncol.* **23**, 2605–2612 (2012).
686 3. Trillsch, F. *et al.* Primary platinum resistance and its prognostic impact in patients with recurrent
687 ovarian cancer: an analysis of three prospective trials from the NOGGO study group. *J. Gynecol. Oncol.* **32**, e37
688 (2021).
689 4. González-Martín, A. *et al.* Newly diagnosed and relapsed epithelial ovarian cancer: ESMO Clinical
690 Practice Guideline for diagnosis, treatment and follow-up. *Ann. Oncol. Off. J. Eur. Soc. Med. Oncol.* **34**, 833–848
691 (2023).
692 5. Baert, T. *et al.* The systemic treatment of recurrent ovarian cancer revisited. *Ann. Oncol.* **32**, 710–725
693 (2021).
694 6. Patch, A.-M. *et al.* Whole-genome characterization of chemoresistant ovarian cancer. *Nature* **521**,
695 489–494 (2015).
696 7. Davidson, B. Biomarkers of drug resistance in ovarian cancer - an update. *Expert Rev. Mol. Diagn.* **19**,
697 469–476 (2019).
698 8. Hoffmann, K. *et al.* Stable expansion of high-grade serous ovarian cancer organoids requires a low-Wnt
699 environment. *EMBO J.* **39**, e104013 (2020).
700 9. Kopper, O. *et al.* An organoid platform for ovarian cancer captures intra- and interpatient
701 heterogeneity. *Nat. Med.* **25**, 838–849 (2019).
702 10. Senkowski, W. *et al.* A platform for efficient establishment and drug-response profiling of high-grade
703 serous ovarian cancer organoids. *Dev. Cell* **58**, 1106-1121.e7 (2023).
704 11. LeSavage, B. L., Suhar, R. A., Broguiere, N., Lutolf, M. P. & Heilshorn, S. C. Next-generation cancer
705 organoids. *Nat. Mater.* **21**, 143–159 (2022).
706 12. Trillsch, F. *et al.* Protocol to optimize the biobanking of ovarian cancer organoids by accommodating
707 patient-specific differences in stemness potential. *STAR Protoc.* **4**, 102484 (2023).
708 13. Riss, T. L. *et al.* Cell Viability Assays. in *Assay Guidance Manual* (eds. Markossian, S. et al.) (Eli Lilly &

16

709   Company and the National Center for Advancing Translational Sciences, Bethesda (MD), 2004).

710   14.   Steg, A. D. *et al.* Stem cell pathways contribute to clinical chemoresistance in ovarian cancer. *Clin.*
711   *Cancer Res.* **18**, 869–881 (2012).

712   15.   Prasetyanti, P. R. & Medema, J. P. Intra-tumor heterogeneity from a cancer stem cell perspective. *Mol.*
713   *Cancer* **16**, 41 (2017).

714   16.   Labidi-Galy, S. I. *et al.* High grade serous ovarian carcinomas originate in the fallopian tube. *Nat.*
715   *Commun.* **8**, 1093 (2017).

716   17.   Snegovskikh, V., Mutlu, L., Massasa, E. & Taylor, H. S. Identification of Putative Fallopian Tube Stem
717   Cells. *Reprod. Sci.* **21**, 1460 (2014).

718   18.   Hu, Z. *et al.* The Repertoire of Serous Ovarian Cancer Non-genetic Heterogeneity Revealed by Single-
719   Cell Sequencing of Normal Fallopian Tube Epithelial Cells. *Cancer Cell* **37**, 226-242.e7 (2020).

720   19.   Dinh, H. Q. *et al.* Single-cell transcriptomics identifies gene expression networks driving differentiation
721   and tumorigenesis in the human fallopian tube. *Cell Rep.* **35**, 108978 (2021).

722   20.   Flesken-Nikitin, A. *et al.* Ovarian surface epithelium at the junction area contains a cancer-prone stem
723   cell niche. *Nature* **495**, 241–245 (2013).

724   21.   Mitoyan, L. *et al.* A stem cell population at the anorectal junction maintains homeostasis and
725   participates in tissue regeneration. *Nat. Commun.* **12**, 2761 (2021).

726   22.   Cohen, E. *et al.* Significance of stress keratin expression in normal and diseased epithelia. *iScience* **27**,
727   108805 (2024).

728   23.   Kim, S., Wong, P. & Coulombe, P. A. A keratin cytoskeletal protein regulates protein synthesis and
729   epithelial cell growth. *Nature* **441**, 362–365 (2006).

730   24.   Khanom, R. *et al.* Keratin 17 Is Induced in Oral Cancer and Facilitates Tumor Growth. *PLoS ONE* **11**,
731   e0161163 (2016).

732   25.   Escobar-Hoyos, L. F. *et al.* Keratin 17 in premalignant and malignant squamous lesions of the cervix:
733   proteomic discovery and immunohistochemical validation as a diagnostic and prognostic biomarker. *Mod.*
734   *Pathol. Off. J. U. S. Can. Acad. Pathol. Inc* **27**, 621–630 (2014).

735   26.   Li, C. *et al.* A pan-cancer analysis of the oncogenic role of Keratin 17 (KRT17) in human tumors. *Transl.*
736   *Cancer Res.* **10**, 4489–4501 (2021).

737   27.   Roa-Peña, L. *et al.* Keratin 17 Testing in Pancreatic Cancer Needle Aspiration Biopsies Predicts Survival.
738   *Cancer Cytopathol.* **129**, 865–873 (2021).

739   28.   Pan, C. *et al.* An unbiased high-throughput drug screen reveals a potential therapeutic vulnerability in
740   the most lethal molecular subtype of pancreatic cancer. *Mol. Oncol.* **14**, 1800–1816 (2020).

741   29.   Bai, J. D. K. *et al.* Keratin 17 is a negative prognostic biomarker in high-grade endometrial carcinomas.
742   *Hum. Pathol.* **94**, 40–50 (2019).

743   30.   Mikami, T. *et al.* Keratin 17 is co-expressed with 14-3-3 sigma in oral carcinoma in situ and squamous
744   cell carcinoma and modulates cell proliferation and size but not cell migration. *Virchows Arch. Int. J. Pathol.*
745   **466**, 559–569 (2015).

746   31.   Hu, H. *et al.* Keratin17 Promotes Tumor Growth and is Associated with Poor Prognosis in Gastric
747   Cancer. *J. Cancer* **9**, 346–357 (2018).

748   32.   DePianto, D., Kerns, M., Dlugosz, A. A. & Coulombe, P. A. Keratin 17 promotes epithelial proliferation
749   and tumor growth by polarizing the immune response in skin. *Nat. Genet.* **42**, 910–914 (2010).

750   33.   Ji, R. *et al.* Keratin 17 upregulation promotes cell metastasis and angiogenesis in colon
751   adenocarcinoma. *Bioengineered* **12**, 12598–12611 (2021).

752   34.   Li, J. *et al.* KRT17 confers paclitaxel-induced resistance and migration to cervical cancer cells. *Life Sci.*
753   **224**, 255–262 (2019).

754   35.   Choi, H. J. *et al.* A novel PI3K/mTOR dual inhibitor, CMG002, overcomes the chemoresistance in
755   ovarian cancer. *Gynecol. Oncol.* **153**, 135–148 (2019).

756   36.   Zhang, D. *et al.* Inhibition of AKT sensitizes chemoresistant ovarian cancer cells to cisplatin by
757   abrogating S and G2/M arrest. *Exp. Mol. Pathol.* **100**, 506–513 (2016).

758   37.   Yu, C., Yu, Q., Lu, J. & Zhou, J. KRT17 enhances carboplatin resistance in ovarian cancer through the

759   AKT/mTOR pathway. https://www.ejgo.net/articles/10.22514/ejgo.2022.032 (2022)
760   doi:10.22514/ejgo.2022.032.

761   38.   Bankhead, P. *et al.* QuPath: Open source software for digital pathology image analysis. *Sci. Rep.* **7**,
762   16878 (2017).

763   39.   Celeste, A. *et al.* Histone H2AX phosphorylation is dispensable for the initial recognition of DNA
764   breaks. *Nat. Cell Biol.* **5**, 675–679 (2003).

765   40.   Farmer, H. *et al.* Targeting the DNA repair defect in BRCA mutant cells as a therapeutic strategy.
766   *Nature* **434**, 917–921 (2005).

767   41.   Zhang, K. *et al.* Longitudinal single-cell RNA-seq analysis reveals stress-promoted chemoresistance in
768   metastatic ovarian cancer. *Sci. Adv.* **8**, eabm1831 (2022).

769   42.   Alisafaei, F. *et al.* Vimentin is a key regulator of cell mechanosensing through opposite actions on
770   actomyosin and microtubule networks. *Commun. Biol.* **7**, 1–13 (2024).

771   43.   Huo, Y. *et al.* Downregulation of vimentin expression increased drug resistance in ovarian cancer cells.
772   *Oncotarget* **7**, 45876–45888 (2016).

773   44.   Wang, M. *et al.* Acquired semi-squamatization during chemotherapy suggests differentiation as a
774   therapeutic strategy for bladder cancer. *Cancer Cell* **40**, 1044-1059.e8 (2022).

775   45.   Flesken-Nikitin, A. *et al.* Pre-ciliated tubal epithelial cells are prone to initiation of high-grade serous
776   ovarian carcinoma. *Nat. Commun.* **15**, 8641 (2024).

777   46.   Budczies, J. *et al.* Cutoff Finder: A Comprehensive and Straightforward Web Application Enabling Rapid
778   Biomarker Cutoff Optimization. *PLoS ONE* **7**, e51862 (2012).

779   47.   Blagden, S. P. *et al.* Phase IB Dose Escalation and Expansion Study of AKT Inhibitor Afuresertib with
780   Carboplatin and Paclitaxel in Recurrent Platinum-resistant Ovarian Cancer. *Clin. Cancer Res. Off. J. Am. Assoc.*
781   *Cancer Res.* **25**, 1472–1478 (2019).

782   48.   Konstantinopoulos, P. A. *et al.* Olaparib and α-specific PI3K inhibitor alpelisib for patients with
783   epithelial ovarian cancer: a dose-escalation and dose-expansion phase 1b trial. *Lancet Oncol.* **20**, 570 (2019).

784   49.   Masson, G. Laekna seeks regulatory path after phase 2 ovarian cancer fail.
785   https://www.fiercebiotech.com/biotech/after-gsk-and-novartis-hand-offs-laeknas-drug-fails-ovarian-cancer-
786   trial (2024).

787   50.   Bapat, S. A., Mali, A. M., Koppikar, C. B. & Kurrey, N. K. Stem and progenitor-like cells contribute to the
788   aggressive behavior of human epithelial ovarian cancer. *Cancer Res.* **65**, 3025–3029 (2005).

789   51.   Cooke, S. L. & Brenton, J. D. Evolution of platinum resistance in high-grade serous ovarian cancer.
790   *Lancet Oncol.* **12**, 1169–1174 (2011).

791   52.   Halim, A.-B. Do We have a Satisfactory Cell Viability Assay? Review of the Currently Commercially-
792   Available Assays. *Curr. Drug Discov. Technol.* **17**, 2–22 (2020).

793   53.   Nair, R. R. *et al.* A role for keratin 17 during DNA damage response and tumor initiation. *Proc. Natl.*
794   *Acad. Sci.* **118**, e2020150118 (2021).

795   54.   Trillsch, F. *et al.* Strategy for Biobanking of Ovarian Cancer Organoids: Addressing the Interpatient
796   Heterogeneity across Histological Subtypes and Disease Stages. *J. Vis. Exp. JoVE* (2024) doi:10.3791/66467.

797   55.   Hierlmayer, S. *et al.* Establishment of Stable Knockdown of MACC1 Oncogene in Patient-Derived
798   Ovarian Cancer Organoids. *Methods Protoc.* **7**, 104 (2024).

799   56.   Batth, T. S. *et al.* Protein Aggregation Capture on Microparticles Enables Multipurpose Proteomics
800   Sample Preparation. *Mol. Cell. Proteomics MCP* **18**, 1027–1035 (2019).

801   57.   Bortel, P. *et al.* Systematic Optimization of Automated Phosphopeptide Enrichment for High-Sensitivity
802   Phosphoproteomics. *Mol. Cell. Proteomics MCP* **23**, 100754 (2024).

803
804

Figure Legends

Figure 1 The Organoid Drug Resistance (ODR) test

(A), Phase contrast images of 4 PDO lines. Scale bars, 500 µm and 100 µm. (B), Individual and (C), Combined log-transformed dose-response curves showing patient-specific differences in sensitivity to carboplatin. Error bars are ± SEM of technical triplicates. Platinum IC50 concentration (µM). (D), Schematic ODR-test workflow illustrating key experimental steps of the assay. (E), Phase contrast images of representative PDO line at 72 h recovery and (F), 7 days post-split (P1) for each concentration (scale bar, 500 µm), green box = GPC for the given line, where long-term expansion was possible. (G), Direct comparison of GPC and IC50 levels in µM for each PDO line. (H), Diagram of normalized organoid counts in P1, Error bars are ±SEM of technical replicates from different wells. (I), mean organoid surface area diagrams showing the distribution of organoids that regrew after the carboplatin challenge. The range is calculated as mean ±SEM. (J), Phase contrast images of 4 ptGPC PDO lines, illustrating sustained long-term expansion >3 months. Scale bars, 500 µm and 100 µm.

Figure 2 *In vitro* modeling of platinum resistance

(A), IF staining of p-BRCA (left) and γ-H2Ax (right) of untreated and ptGPC PDOs showing sustained DNA damage and activation of DNA repair in pre-exposed lines. Scale bars, 20 µm and 10 µm. (B), qPCR of expression of stemness- and differentiation-related target genes in ptGPC organoids (n=4 independent biological sample pairs). Error bars ± SEM. (C),(D), IF staining showing changes in the organization of cytoskeleton (phalloidin, green), nuclear morphology (DAPI, blue), and nucleolus (fibrillarin, red) in untreated vs. ptGPC PDOs. Scalebar, 20 µm, 10 µm and 5 µm. (E), Schematic ODR2-test workflow for the rechallenge of the ptGPC1 organoids. (F), Direct comparison of 7 days P1 phase contrast images for the representative donor line after ODR1 and ODR2 test, showing differences in sensitivity/growth potential (scale bars, 500 µm, and 100 µm) leading to (G), increasing GPC (GPC1 to GPC2 comparison in µM), for three pairs of PDO lines. (H), Quantification of the change in drug sensitivity, measured by organoid count, normalized to the control for ODR1, and ODR2. Scale bars are ±SEM of technical triplicates, and P-values are calculated by the Student t-test (*p <0,05, **p<0.01; ***p<0.001, **** p<0,001).

Figure 3 Post-Platinum organoid transcriptomic and proteomic characterization

(A), PCA plot of mRNA sequencing of control vs. GPC lines, for two donors, showing patient-specific characteristics dominating expression profiles of the organoids. (B), Volcano plot of top 25 regulated candidate genes (Log2 Foldchange, p-adjust < 0.05). (C), heat-map analysis of the top 25 regulated genes (p-adjust < 0.05), illustrates that despite great differences between donors samples cluster according to treatment. (D), GSEA for GO Biological processes in untreated vs. ptGPC1 lines identifies enrichment in pathways regulating cytoskeleton and differentiation. (P-adjust< 0,05). (E), PCA plot of mass spectrometry measurements (n=4 independent technical replicates for two sets of lines ctrl vs GPC, total 16 samples), confirms that patient-specific characteristics are defining components in the global proteome profile. (F), GSEA of top enriched pathways for proteome (NES), identifies enrichment in downregulation for pathways regulating cell adhesion and locomotion. (G), ES plots for cell adhesion in transcriptome and proteome data. (H), Loss of vimentin IF staining visualized by confocal imaging. ptGPC1 organoids in comparison to the control line. Scale bar, 20 µm. (I), qPCR validation of the induction of KRT17 in ptGPC1 organoids (n=3 independent biological samples) and (J), by IF staining in confocal imaging. Scalebar, 20 µm.

19

850

Figure 4 Platinum hyper resistance by KRT17 editing

(A), qPCR of individual KRT17 exons, in control vs. crKRT17 edited lines shows loss of expression of exon 4 (n=3 independent biological replicates). Errorbar ±SEM. (B), Western blot for KRT17 confirms expression of the truncated protein. (C), Comparative phase contrast images after ODR2-test for WT crKRT17 lines illustrating long-term expansion potential after sustaining 25 µM and 100 µM challenge in P0. Scale bars, 500 µm. (D), Bar plot summarizing shift in GPC levels and a strong increase in crKRT17 line. (E), KRT17 RNA expression by qPCR of treated and untreated, WT and crKRT17 lines, illustrates strong induction in the expression of KRT17 in crKRT17 organoids (n=3 independent biological samples). Errorbars ±SEM. (F), Mass spectrometry data show a significantly lower or absent MS/MS intensity of the DAEDWFFSK peptide, corresponding to the coding region of exon 4, in edited organoid lines compared to total KRT17 protein intensity (n=4 independent biological samples), confirming the overexpression of the remaining portion of the protein in ptGPC2 organoids. (G), Confocal imaging validates a strong increase in KRT17 levels and (H), KRT5 levels. Scalebars, 20 and 50 µm. (I), Re-distribution of Occludin staining signal to lateral membranes in crKRT17 ptGPC2 organoids indicates loss of polarity. Scalebar, 50 µm and 25 µm. (J), Western blot for KRT17 expression in KI-KRT17 and control lines, with Flag and endogenous KRT17 antibody, confirms expression of the exogenous construct as well as induction of endogenous protein in response to carboplatin. (K), Phase contrast images of control and KI-KRT lines at two different carboplatin concentrations (25 µm and 50 µm) at P1. Scalebars, 100 µm. (L), Quantification of the ODR1-test of KI-KRT17 vs. lenti-ctrl organoids showing the increase in organoid counts and rise in GPC. GPC1=25 µM (lenti-ctrl) and GPC1=50 µM (KI-KRT17). Scalebars, 100 µm. (M), Analysis of the distribution of organoid sizes reveals a group of significantly larger organoids (dotted circles) in ptGPC KI KRT17 culture suggestive of increased stemness potential. Error bars ±SEM of measurements in independent wells. P-values are calculated by the Student t-test for the quantification of organoid counts, and the Mann-Whitney U test for comparison of differences in organoid sizes (*p <0,05, **p<0.01; ***p<0.001, **** p<0,001).

Figure 5 Prognostic K-score as stratification to PIK3/Akt-targeted therapy

(A), Images of KRT17 immunohistochemical staining representing TMA cores of 5 exemplary patients displaying different levels of expression. (B), Kaplan-Meier analysis in the patient cohort of advanced HGSOC cases. K-score cutoff, 5 %. Reveals significantly shorter OS (p-value (Log-Rank) = 0.0043) and (C), PFS (p-value (Log-Rank) = 0.008) for the group of KRT17^{high} patients. (D), Multivariate Cox regression analysis for OS and (E), for PFS, confirms the prognostic value of the K-score as an independent risk factor (HR 1.84, p-value=0.008 for OS, and HR 1.58, p-value=0.024) for PFS. (F), log-transformed dose-response curves for alpelisib in untreated and carboplatin-treated WT and crKRT17 lines, show a strong increase in sensitivity in the lines expressing elevated KRT17 levels. (G), IC50 values in µM, in independent biological replicates of the assay and (H), (I), showing results of the analogous testing setup for afuresertib. (K), Alpelisib treatment of the KI-KRT17 expressing independent donor line confirms the capacity of KRT17 to directly modify the sensitivity of the organoids to PI3 kinase pathway inhibition. Error bars are ±SEM of technical triplicates.
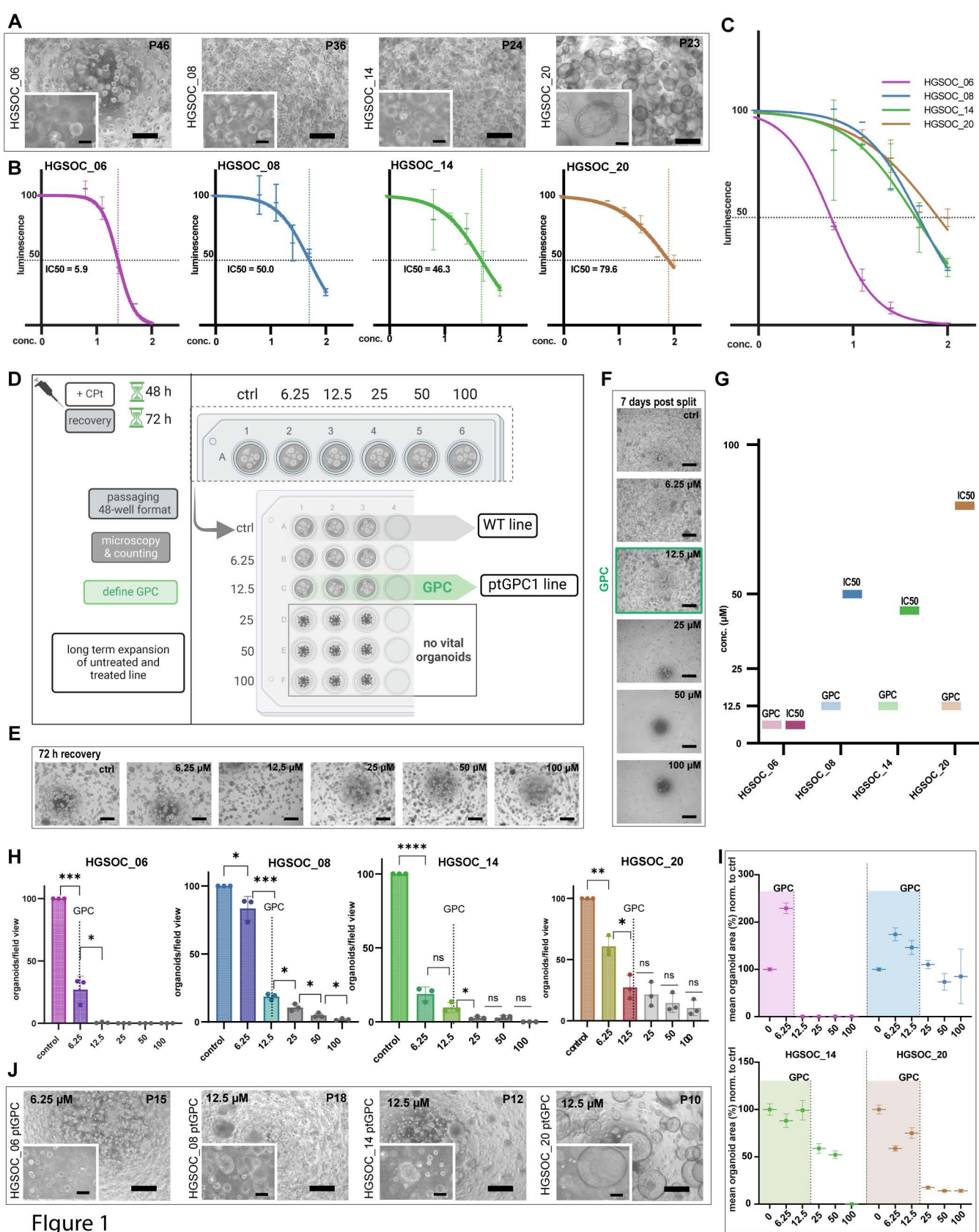
Figure 1

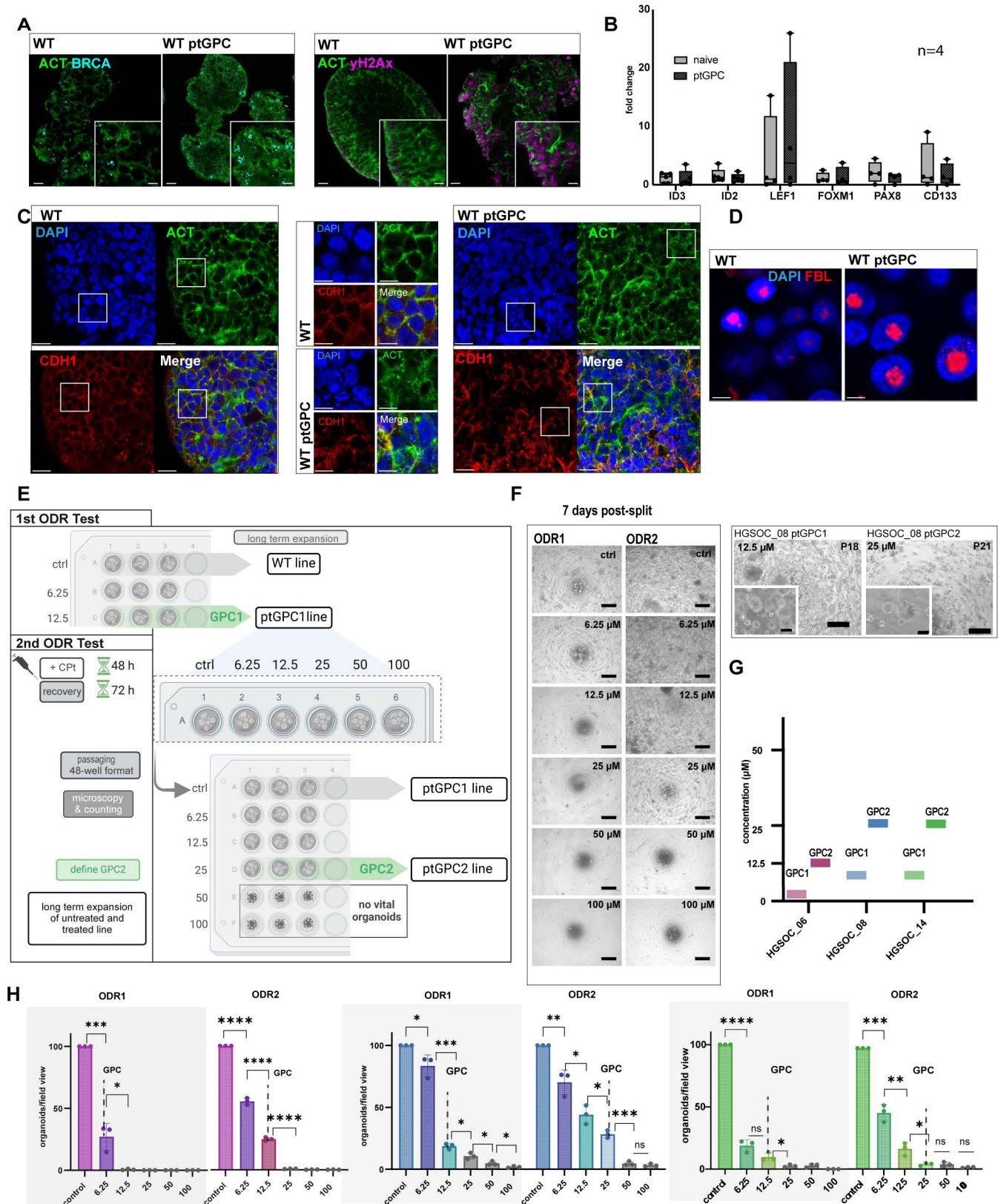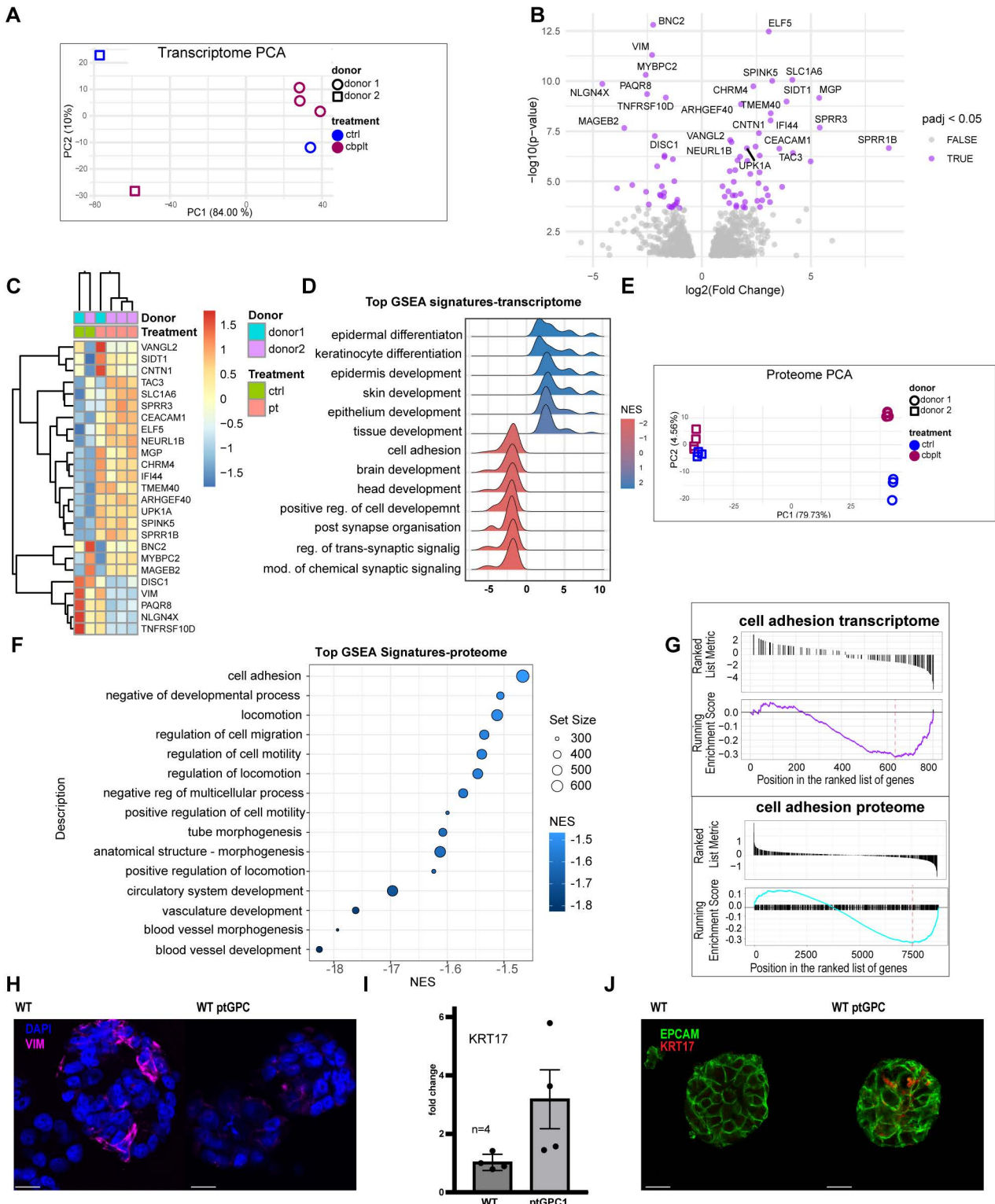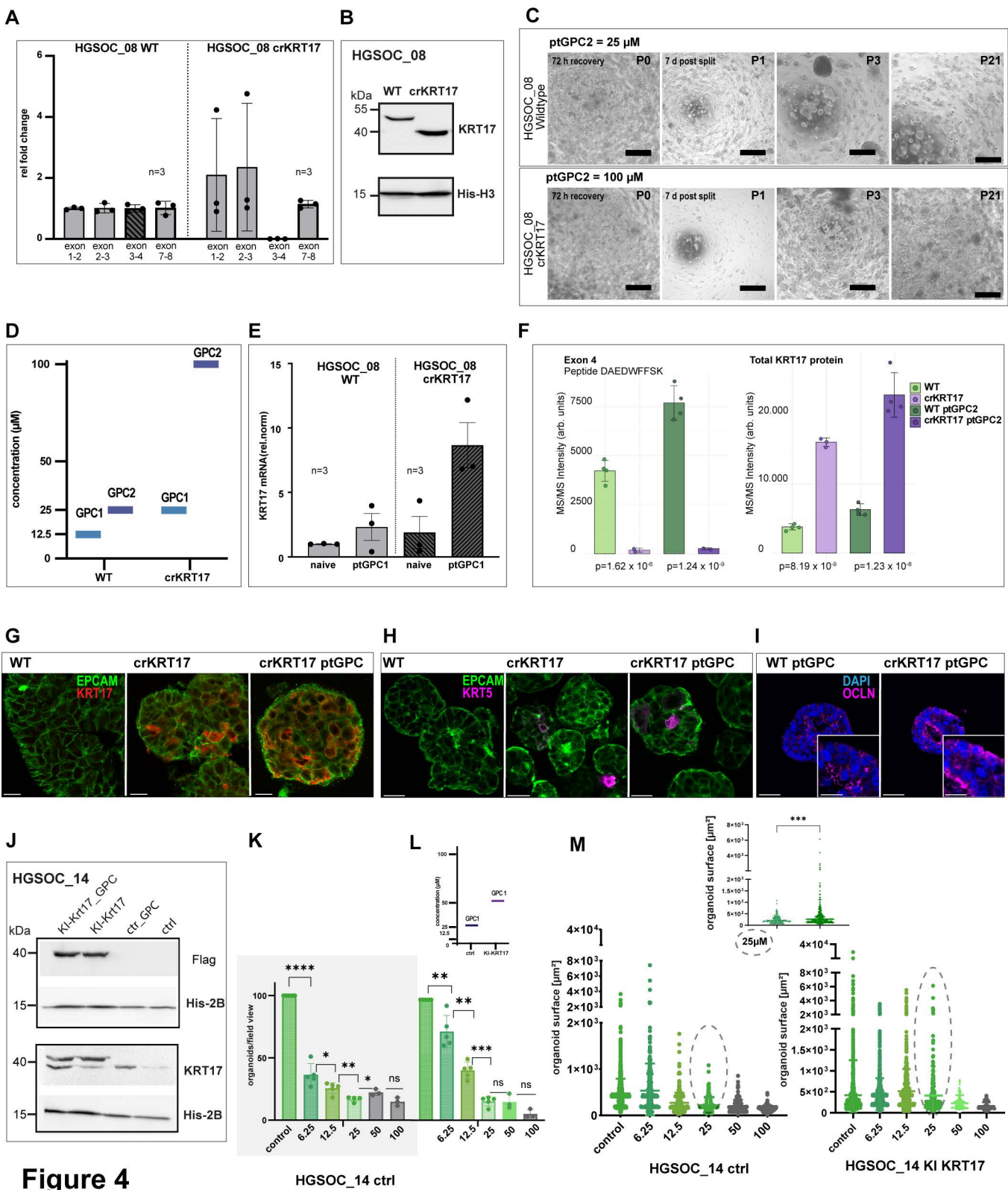**Figure 2**

Figure 3

Figure 4

A

patient 1 — K-Score 0.07
patient 2 — K-Score 5.56
patient 3 — K-Score 14.87
patient 4 — K-Score 27.43
patient 5 — K-Score 77.95

negative ——— K-Score ——— positive

B Overall Survival for HGSOC FIGO III-IV

Median OS (95 % CI)
K-Score < 5 % 41 months (35.3-46.7)
K-Score > 5 % 21 months (11.1-30.9)

P-value (Log Rank) = 0.0043

Probability of overall survival

patients at risk

< 5 %	335	102	23
> 5 %	41	7	1

Time (months)

C Progression Free Survival for HGSOC FIGO III-IV

Median PFS (95 % CI)
K-Score < 5 % 19 months (17.1-20.9)
K-Score > 5 % 14 months (10.9-17.2)

P-value (Log Rank) = 0.0081

Probability of progression free survival

patients at risk

< 5 %	335	48
> 5 %	41	2

Time (months)

D

Hazard ratio for OS

K-Score </> 5 % (N= 376)	1.84 (1.17-2.87)	0.008**
Surgical macroscopic tumorrest (N= 376)	1.45 (1.21-1.74)	< 0.001***
Primary/debulking surgery (N= 376)	0.81 (0.46-1.41)	0.459
ASA Status (N= 299)	1.72 (1.28-2.32)	< 0.001***
Age </> 60 years (N= 376)	0.56 (0.40-0.79)	0.001**

E

Hazard ratio for PFS

K-Score </> 5 % (N= 376)	1.58 (1.06-2.34)	0.024*
Surgical macroscopic tumorrest (N= 376)	1.27 (1.09-1.48)	0.002**
Primary/debulking surgery (N= 376)	1.16 (0.77-1.74)	0.472
ASA Status (N= 299)	1.26 (1.00-1.59)	0.049*
Age </> 60 years (N= 376)	0.75 (0.58-0.96)	0.024*

F Alpelisib

n=2

luminescence

WT naive IC50 = 15.26 µM
WT exOFE2 IC50 = 15.53 µM
crKRT17 naive IC50 = 9.89 µM
crKRT17 exOFE2 IC50 = 5.77 µM

log(conc)

G Afuresertib

n=2

luminescence

WT naive IC50 = 18.51 µM
WT exOFE2 IC50 = 15.83 µM
crKRT17 naive IC50 = 10.70 µM
crKRT17 exOFE2 IC50 = 9.17 µM

log(conc)

H Alpelisib in KI-KRT17

luminiscence

HGSO14_KI-KRT17 IC50=9,97 µM
HGSOC14_Ctrl IC50=17,96 µM

log(conc)

Figure 5